

Development of a technique for the precise determination of atomic lifetimes based on photon echoes

H. C. Beica^{✉,*}, A. Pouliot[✉], P. Dowling, A. Carew, T. Vacheresse, G. Carlse, L. Marmet[✉], and A. Kumarakrishnan[†]
Department of Physics and Astronomy, York University, 4700 Keele Street, Toronto, Ontario, Canada M3J 1P3

 (Received 26 June 2019; accepted 24 February 2020; published 16 March 2020)

We explore the sensitivity of the photon echo technique for achieving precise measurements of atomic lifetimes. Using short-pulse excitation of atomic rubidium vapor, we report the most statistically precise measurement of (26.11 ± 0.03) ns for the $5^2P_{3/2}$ lifetime. This statistical uncertainty of 0.11% was achieved in a total data acquisition time of 4 h over several weeks and rivals the most precise measurements in this atomic system. The experiment primarily relies on heterodyne detection and exploits the signal-to-noise ratio of the coherent release of energy along the direction of excitation, which is an exponential decay as a function of pulse separation T , as well as large repetition rates that are feasible in a gently heated vapor cell. We have developed an understanding of the technical limitations responsible for lifetime measurement instabilities on the basis of a simple model, which also enables us to propose a feedback scheme to limit these effects. Studies of the fractional uncertainty of the lifetime suggest that the statistical precision of this technique can be extended to the level of 0.03% in 10 min of data acquisition if the technical limitations are addressed. This level of precision has so far been exceeded by only one other lifetime measurement. Under these conditions, a rigorous investigation of systematic effects could potentially allow the echo technique to achieve the most accurate measurement of atomic lifetimes.

DOI: [10.1103/PhysRevA.101.033408](https://doi.org/10.1103/PhysRevA.101.033408)

I. INTRODUCTION**Overview of lifetime measurements**

Atomic lifetime measurements are used to confirm theoretical predictions for atomic level structure such as dipole matrix elements, polarizabilities, and binding energies. In recent years, increases in computational power have allowed accurate, relativistic, many-body perturbation-theory calculations of not only lower levels of hydrogenlike atoms, but also properties of upper levels of heavier atoms. The calculations are widely used for interpretation of spectroscopic signatures in a variety of applications, ranging from astrophysics to industry [1–3]. The best lifetime measurement to date (based on photoassociation) has achieved a statistical uncertainty of 0.007% and a systematic uncertainty of 0.03% [4], whereas the characteristic accuracy of other commonly used techniques is about 0.2% [5–8]. However, the accuracy of theoretical calculations [1–3] is at the level of 1.6%. These experiments involve measurements of the natural linewidth (on the order of a few megahertz in alkali-metal atoms) using absorption spectroscopy [7] or studies of radiative lifetime in samples such as laser-cooled atoms [5,7] and atomic beams [6]. The most prominent systematic effect in absorption measurements is the laser linewidth, making it necessary to develop lasers with kilohertz linewidths [7]. For measurements of radiative lifetimes, it is necessary to operate at low densities to avoid the effects of radiation trapping, thereby making it essential to develop photon-counting techniques that can result in longer data acquisition times [5,6]. Both types of

measurements have additional complexities associated with sample preparation such as state selection of atoms, non-magnetic setups for atom trapping, and highly collimated atomic beams that need to be spatially imaged so that the distance over which excited atoms fluoresce can be converted to time from the knowledge of the speed distribution [6]. Other motivations for accurate lifetime measurements [9,10] and their comparison with theory [11,12] are related to tests of the standard model involving parity nonconservation. Table I shows a comparison of leading atomic lifetime measurements. Such comparisons can be further validated by performing measurements using experimental techniques with different systematic effects [13–16].

Another well-established technique that has been extensively exploited to measure relaxation effects in solids [17–19], collisional relaxation in gases [20,21], and molecular lifetimes [22] is based on optical photon echoes [21,23,24]. A photon echo experiment can eliminate many of the aforementioned specialized requirements for atomic lifetime measurements. Such an experiment requires the excitation of a two-level atomic system by two traveling-wave pulses that are temporally separated by $t = T$. The first pulse prepares a coherent superposition of ground and excited states, which produces coherent radiation along the direction of the excitation pulse. In a classical description, the radiation terminates due to Doppler dephasing when the individual atoms of a dilute gas travel a distance larger than the wavelength of light. The duration of this transient signal, known as free induction decay (FID), is on the order of $\lambda/u = 1$ ns in a room-temperature gas of Rb atoms, where u is the most probable speed and λ is the wavelength of light. However, if the excited state has not decayed, a second excitation pulse can rephase the superposition state at a time $t = 2T$, resulting in a burst of

*hceica@gmail.com

†akumar@yorku.ca

TABLE I. Comparison of lifetime measurements achieved by leading techniques. The last two entries represent the most accurate theoretical calculations.

Reference	Technique	Rb lifetime measurements	Accuracy
Oates <i>et al.</i> [7]	Linewidth of laser-cooled atoms (Na)	N/A	0.25%
Volz <i>et al.</i> [6]	Supersonic atomic beams (Li, Na, K, Rb)	$5P_{1/2}$: 27.70(4) ns $5P_{3/2}$: 26.24(4) ns	0.14–0.25%
Simsarian <i>et al.</i> [5]	Photon counting in atom trap (Fr and Rb)	$5P_{1/2}$: 27.64(4) ns $5P_{3/2}$: 26.20(9) ns	0.15–0.37%
Young <i>et al.</i> [10]	Photon counting in atomic beam (Cs)	N/A	0.2–0.3%
McAlexander <i>et al.</i> [4]	Cold atom photoassociation (Li)	N/A	0.03%
Gutterres <i>et al.</i> [8]	Photoassociation spectroscopy in ^{87}Rb	$5P_{1/2}$: 27.75(8) ns $5P_{3/2}$: 26.25(8) ns	0.3%
Safronova <i>et al.</i> [1,2] ^a	Relativistic perturbation theory in Rb	$5P_{1/2}$: 26.82 ns $5P_{3/2}$: 26.44 ns	N/A
Safronova <i>et al.</i> [3] ^b	Relativistic perturbation theory in ^{87}Rb	$5P_{1/2}$: 27.4(4) ns $5P_{3/2}$: 26.0(4) ns	1.58% 1.60%

^aLifetimes calculated from reduced dipole matrix elements in Table V of Ref. [1] and Table I of Ref. [2].

^bLifetimes and uncertainties calculated from Einstein A coefficients of Table III in Ref. [3].

radiation known as a photon echo. The radiation associated with the FID and the photon echo is analogous to coherent emission from a phased array of dipole oscillators. The main limitation on the time scale of the experiment is the radiative lifetime of the excited state. Therefore, the exponential decay of the echo intensity (energy radiated by the system) as a function of T can be used to infer the radiative lifetime τ_1 , as illustrated in Fig. 1.

A striking aspect of the photon echo technique is that the coherent emission is directional, with a signal strength that can be many orders of magnitude larger than the signals used in lifetime measurements that rely on monitoring isotropic spontaneous emission. Other advantages are that it does not impose stringent requirements on the laser linewidth. Since the time scale of the measurement is less than 500 ns, it is sufficient to ensure that the excitation pulses are phase coherent over this time period. Consequently, the experiment does not require the kilohertz-linewidth lasers used in other work [7]. A narrow laser linewidth becomes unnecessary

because the pulse bandwidth—which is significantly larger than the laser linewidth—determines the fraction of excited atoms under the Doppler profile. Although typical laser phase noise can be expected to weakly impact the decay time of the echo intensity, it is still necessary to quantify this effect. Most significantly, like other vapor-cell experiments [25], the photon echo technique has the potential for realizing data acquisition with a large repetition rate. Furthermore, the experiment is not sensitive to radiation trapping. This is because the sample density, which can affect the propagation of the echo pulse [24,26], does not impact the total energy as a function of T that is used in the lifetime measurement. Moreover, the sensitivity relies on the ability to measure the energy radiated as a function of precisely incremented delay times T , and not on details such as the onset times of the excitation pulses or the time occurrence of the echo signal. Despite these advantages, this technique appears to have been largely overlooked for precision measurements of atomic lifetimes [24,27].

The first measurement of the $5P_{3/2}$ excited state lifetime in Rb vapor using the photon echo technique reported a “double-blind” lifetime value of (26.5 ± 0.3) ns using excitation pulses with a $1/e^2$ full width of 20 ns [27]. This preliminary measurement involved recording 300 points on the exponential decay, with each point being averaged 128 times at a repetition rate of 20 Hz, resulting in a measurement time of 1 h. The characteristic precision of a single data set was $\sim 10\%$, and in the absence of systematic effects, 72 h of data acquisition were required to produce the 1% accuracy. The agreement of this result with the best measurement in Rb [5,6,8] served as an impetus for this work. Here, we explore the sensitivity of the echo technique and its potential for realizing the most accurate measurement of any atomic lifetime. We use excitation pulses with a 12-ns $1/e^2$ full width to reduce the effects of spontaneous emission during excitation, and a data acquisition system that can operate the experiment at a repetition rate of up to 1 MHz to measure the $5P_{3/2}$ excited-state lifetime in ^{85}Rb . We report a transit-time corrected lifetime value of (26.11 ± 0.03) ns based on 4 h of data acquisition over several weeks, which is in agreement with Ref. [5], but disagrees with Refs. [6,8]. The statistical precision of 0.11% is based on an Allan deviation (ADEV) analysis of the data. We find that this measurement is dominated by noise sources that occur on time scales longer than 50 ms. These noise sources

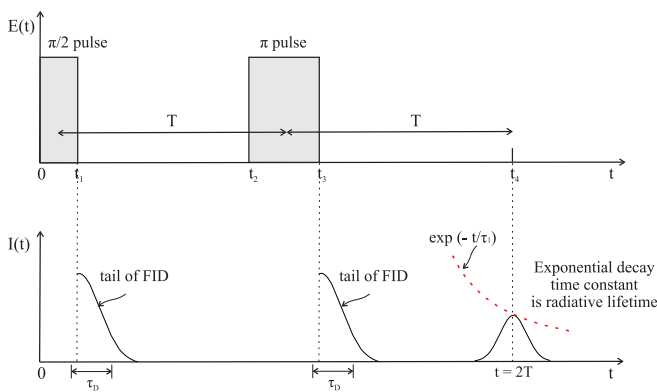


FIG. 1. Top figure shows an idealized representation of two square $\pi/2$ and π excitation pulses with their centers separated by $T = (t_3 + t_2 - t_1)/2$. Here, t_{21} represents the time between the trailing edge of pulse 1 and the rising edge of pulse 2. Similarly, t_{43} represents the time between the falling edge of pulse 2 and the center of the echo pulse. The bottom figure shows the FID due to each pulse and an echo signal at $t = 2T$. The second pulse can be applied even a long time after the FID to rephase the atoms in the excited state, as long as this state has not decayed. The exponential decay time constant τ_1 of the echo intensity is measured as a function of T .

produce variations in the lifetime values that limit a conclusive study of systematic effects. Nevertheless, we find that none of the experimental control parameters produce changes in the lifetime value larger than the statistical uncertainty. We attribute the source of the long-term variations to imperfect background subtraction of excitation pulse tails and present a simple model that supports these conclusions. The model also suggests a practical approach for reducing the long-term variations. Our studies of the fractional uncertainty in the lifetime suggest that the repetition rate achievable in this experiment can result in a statistical precision of 0.03% in ~ 10 min of data acquisition time, which would allow a rigorous study of systematic effects at the same level.

In Sec. II of the paper we provide the theoretical background to interpret our results. Section III describes the experimental setup and the data acquisition system. In Sec. IV, we discuss the results of the measurement. Section V presents a simple model that supports our understanding of the technical limitations and proposes a modified experimental setup that can address these effects.

II. THEORY

An analytical treatment for calculating the echo intensity is given in Ref. [24]. This treatment is based on the optical Bloch equation model for a two-level atom in a rotating frame, as described by the following torque equation:

$$\frac{d\rho}{dt} = \Omega' \times \rho. \quad (1)$$

Here, the Bloch vector $\rho = (u, v, w)$ has components u and v that represent the in-phase and in-quadrature components of the dipole moment, respectively; w is the population difference between the ground and excited states, and the components of the generalized Rabi frequency are given by $(-\Omega, 0, \Delta)$ so that $\Omega' = \sqrt{\Omega^2 + \Delta^2}$, where the Rabi frequency is represented by Ω and the detuning is represented by $\Delta = \omega - \omega_0$. Here, ω is the driving frequency and ω_0 is the resonant frequency. This model does not include the effects of spontaneous emission and pulse propagation. The time-dependent solutions to Eq. (1) can be obtained on the basis of successive rotational transformations which give

$$\begin{bmatrix} u(t) \\ v(t) \\ w(t) \end{bmatrix} = \begin{bmatrix} \frac{\Omega^2 + \Delta^2 \cos \Omega' t}{\Omega^2} & \frac{-\Delta}{\Omega'} \sin \Omega' t & \frac{-\Delta \Omega}{\Omega'^2} (1 - \cos \Omega' t) \\ \frac{\Delta}{\Omega'} \sin \Omega' t & \cos \Omega' t & \frac{\Omega}{\Omega'} \sin \Omega' t \\ \frac{-\Delta \Omega}{\Omega'^2} (1 - \cos \Omega' t) & \frac{-\Omega}{\Omega'} \sin \Omega' t & \frac{\Delta^2 + \Omega^2 \cos \Omega' t}{\Omega'^2} \end{bmatrix} \begin{bmatrix} u_0 \\ v_0 \\ w_0 \end{bmatrix}. \quad (2)$$

Here, u_0, v_0, w_0 represent the initial values of the Bloch vector and $\Omega = 2dE_0/\hbar$ is the Rabi frequency specified in terms of the electric-field amplitude E_0 and the dipole moment d . The solutions represented by Eq. (2) impose no limit on the value of the Rabi frequency and can model the time-dependent Bloch vector components for a wide range of experimental conditions, including on-resonant and far-off resonant excitation. Equation (2) can be simulated with the inclusion of spontaneous emission and the spatial profile of the excitation beam [27]. For delta-function excitation pulses, the ratio of pulse areas $r = \theta_2/\theta_1$ (where θ_1 and θ_2 are the areas of the first and second pulse, respectively) required for the maximum echo intensity has a value of 2, corresponding to a $\pi/2, \pi$ pulse sequence [24]. Simulations of Eq. (2) with either square pulses or Gaussian pulses show that r has a value of 1.89 and 1.70, respectively. For Gaussian-pulse excitation, the value of r is further reduced to 1.44 if spontaneous emission is included through the introduction of phenomenological decay terms added to Eq. (2). These results are in general agreement with the experimental value of 1.2 obtained with excitation pulses with a $1/e^2$ full width of 20 ns [27].

For square-pulse excitation (Fig. 1) in the limit that $\Omega \gg \Delta$, Eq. (2) can also be used to obtain an analytical expression for the atomic polarization density of the photon echo [24], as given by

$$P(t_4) = -\xi d \sin(\omega + \Delta)t_4 \exp \left[-\frac{\pi}{4} \left(\frac{t_{43} - t_{21} - 1/\Omega}{T_2^*} \right)^2 \right], \quad (3)$$

where ξ is the number density, and the time delays t_{21} and t_{43} are defined for the case of square-pulse excitation in Fig. 1. If $1/\Omega \ll T$, this equation predicts that the duration of the echo signal envelope is dominated by the inhomogeneous (Doppler dephasing) time T_2^* . If the excitation pulse bandwidth only excites a fraction of the Doppler width, the value of T_2^* becomes the pulse width. The polarization density in Eq. (3) can be used as the source term in the wave equation given by

$$\frac{\partial^2 E(x, t)}{\partial x^2} - \frac{1}{c^2} \frac{\partial^2 E(x, t)}{\partial t^2} = \mu_0 \frac{\partial^2 P(x, t)}{\partial t^2}. \quad (4)$$

In the presence of spontaneous emission, the echo intensity I (at $t = 2T$) can be obtained from the propagated electric field given by Eq. (4). If a phenomenological decay rate $1/\tau_1$ is included to account for spontaneous emission, the echo intensity can be modelled as

$$I = I_0 \exp \left[-\frac{2T}{\tau_1} \right], \quad (5)$$

where I_0 is the peak intensity. This model ignores the effects of other dephasing mechanisms, such as the effect of collisions, as well as corrections due to the transit time of atoms through the excitation beam. Reference [24] predicts small deviations in the echo time in the vicinity of $t = 2T$ for specific pulse areas. However, in the experiment, we integrate the echo intensity over the echo envelope and plot the resulting energy as a function of $2T$ to measure τ_1 .

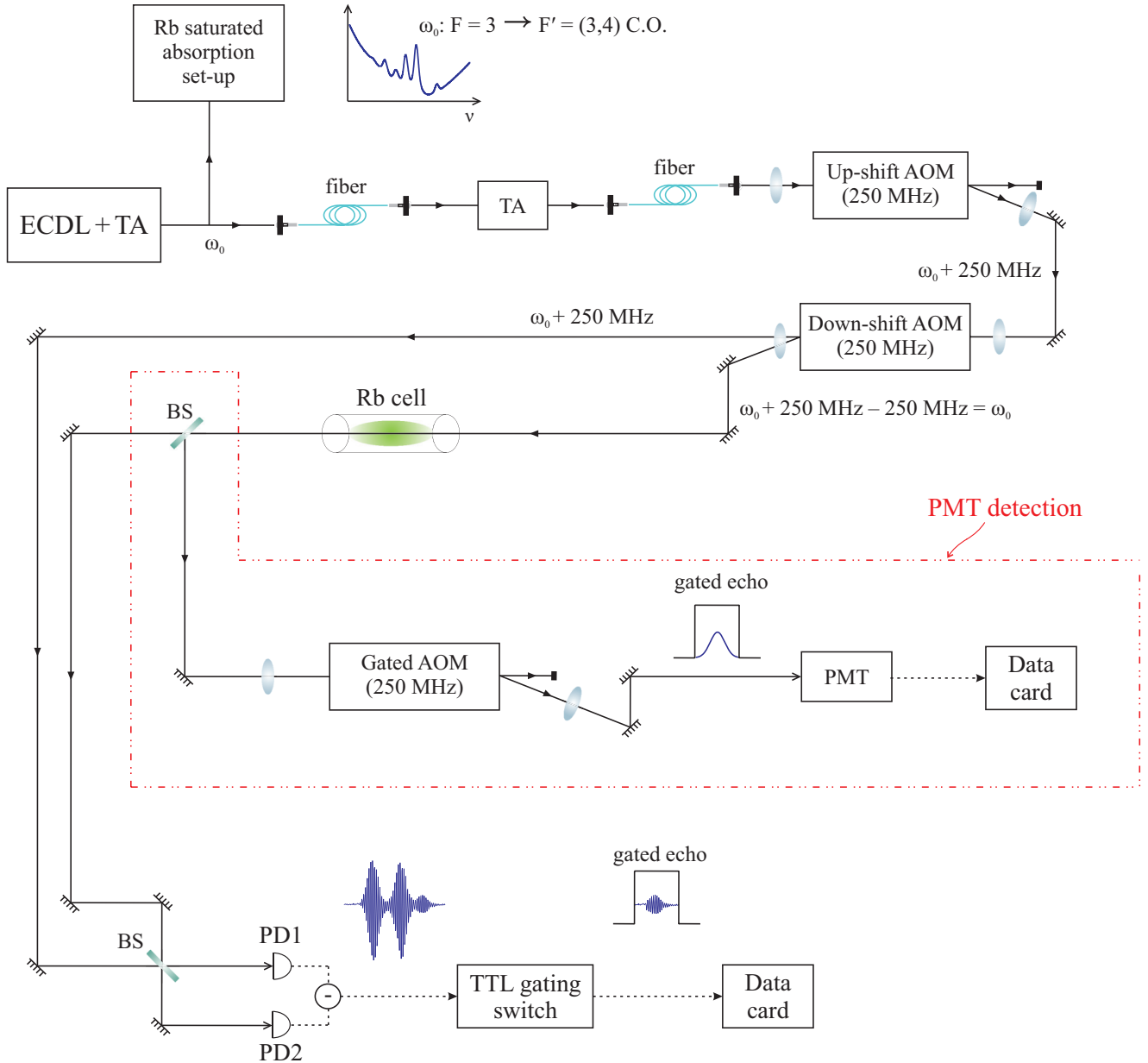


FIG. 2. Experimental layout showing the seed laser, TA, AOM chain, and heterodyne detector. ω_0 designates a crossover (C.O.) resonance. The dashed lines show the experimental layout involving PMT detection.

III. EXPERIMENTAL DETAILS

The key requirements for this experiment include excitation pulses that are comparable to or shorter than the atomic lifetime (~ 26 ns), the reduction of background light so that the atomic coherences remain unperturbed during the measurement, rapid data acquisition to avoid long-term noise sources that can contribute to lifetime measurement variations, and detection systems that can avoid saturation and still temporally resolve an echo signal that is approximately 1000 to 1 00 000 times smaller in intensity than the excitation pulses. Additionally, the spatial profile of the excitation beam should be sufficiently large to minimize transit-time corrections to the atomic lifetime, while still ensuring adequate atom-field coupling strengths for the excitation pulses to

compensate for vapor absorption and spontaneous emission during excitation. The experiment exploits the benefits of a fiber-coupled master oscillator power amplifier (MOPA) laser system [28] coupled through a chain of acousto-optic modulators (AOMs) to generate short pulses. The signal detection is accomplished by either a balanced heterodyne detector with an electronic gate or a photomultiplier tube (PMT) gated by an AOM.

The experimental setup is shown in Fig. 2. We use an external cavity diode laser (ECDL) that is frequency stabilized to the $F = 3 \rightarrow F' = (3, 4)$ crossover resonance, as well as to neighboring resonances within the Doppler profile in ^{85}Rb , using a saturated absorption spectrometer with a room-temperature Rb vapor cell that is 5 cm in length. The 50-mW output of the ECDL is amplified to 200 mW by a tapered

amplifier (TA) and fiber-coupled so that it can seed a number of TAs simultaneously. References [29,30] show that the spectral characteristics of the amplified light are well matched with those of the seed laser. The photon echo experiment relies on a TA with a 30-mW fiber-coupled input to produce an output of 1.7 W. After passing through a Faraday isolator and beam-shaping lenses, this beam is spatially filtered to reduce amplified spontaneous emission using an optical fiber. The fiber-coupled output of 400 mW is aligned through two successive AOMs operating at 250 MHz. The first (“upstream”) AOM produces an upshift of 250 MHz and operates in the Bragg regime with a gently focused laser beam to achieve a diffraction efficiency of $\sim 70\%$. This AOM provides a gate pulse for the experiment (full width at half maximum of 500 ns) to suppress background light from going into the experiment. The second (“downstream”) AOM is aligned to produce a downshift of 250 MHz. The laser beam is focused to a spot size of $\sim 30 \mu\text{m}$ through this AOM to generate Gaussian pulses with a $1/e^2$ intensity full width of 12 ns. As a result, the diffraction efficiency is reduced to $\sim 35\%$, which ensures that the excitation beam has a peak power of 100 mW. The diffracted beam from the downstream AOM is thus tuned back to the original lock point, which is within the Doppler profile of the $F = 3 \rightarrow F' = 2, 3, 4$ transitions. Both the upstream and the downstream AOMs are pulsed to generate the two-pulse excitation sequence. The excitation beam has an elliptical spatial profile with $1/e^2$ half widths of $\sim 1.5 \times 1.0 \text{ mm}^2$ (with an estimated uncertainty of 10%). From the peak intensity and the average beam radius, we estimate that the maximum pulse area for a second excitation pulse with a $1/e^2$ full width of 12 ns to be $\sim 15\pi$. The ratio r of the areas of the excitation pulses ranges from 1.3 to 1.5. The first-order diffracted beam of the downstream AOM is sent through a 10-cm-long Rb cell. Since the excitation pulses are collinear, the echo is emitted along the same direction. The cell is surrounded by heating tape and insulated so that its temperature can be increased and stably maintained to $\pm 1^\circ\text{C}$. We generally operate at a temperature of $\sim 40^\circ\text{C}$, at which the Rb vapor pressure is $\sim 3 \times 10^{-6}$ Torr. The insulated cell is placed inside a solenoid with no magnetic shielding. The maximum magnetic field along the direction of excitation can be varied from +20 to -20 G. It is also possible to vary the polarization of the excitation beam from linear to circular with the use of wave plates.

For the heterodyne detection setup shown in Fig. 2, the undiffracted beam from the downstream AOM serves as a local oscillator (LO), which is aligned parallel to the excitation beam (diffracted beam from downstream AOM) outside of the Rb cell. Since the LO frequency is upshifted with respect to the excitation beam, this configuration ensures that any background light that scatters into the cell from the LO only interacts weakly with the Doppler-broadened transition. The electric field of the photon echo signal is detected by overlapping with the LO to generate a 250-MHz beat note, which is recorded by a pair of balanced PIN photodiodes (1-ns rise time) in an optical heterodyne setup. The output of the heterodyne detector is sent into a 25-dB rf amplifier and gated by a transistor-transistor logic (TTL) switch so that only the echo signal is sent to the data card. In the alternate detection scheme, the echo intensity is recorded on a PMT with a rise

time of 1 ns. An additional 250-MHz AOM is used to gate the echo signal so that the PMT is not exposed to the excitation pulses, as shown in the dashed region of Fig. 2.

The two AOMs are operated by a phase-locked voltage-controlled 250-MHz oscillator slaved to a 10-MHz Rb clock with an ADEV of 5×10^{-13} at 5000 s [31]. The 10-MHz signal also slaves the time base of the delay generator that controls the gating pulse of the upstream AOM and the two excitation pulses of the downstream AOM. Under these conditions, the leading edges of the pulses can be set to a precision of 1 ps. The AOMs are controlled by an rf network consisting of TTL switches with an extinction ratio of 80 dB, power splitters, mixers, and rf isolators. The excitation pulses are generated by varying the amplitude and width settings of the pulse generator to optimize the echo amplitude. The protocol to measure the echo signal involves temporally overlapping two identical excitation pulses, identifying the minimum value of T (defined as the time separation between the leading edges of the rf excitation pulses) at which the echo signal is approximately twice the $1/e^2$ full width of the second pulse, and then adjusting the excitation pulse amplitude and widths to maximize the signal without consideration of pulse areas. Subsequently, the time delay T between the leading edges of the excitation pulses are randomly selected between the minimum value and the maximum value at which the signal size is comparable to the background.

The echo signal is detected by a data card with an acquisition rate of 1 GS/s. The card is triggered by the pulse generator 100 ns before the onset of the echo, whereupon it acquires 256 points (256 ns) before re-arming for the next trigger. The card can be configured to operate at repetition rates of up to 1 MHz. The time base of the data card is also slaved to the Rb clock. A C++ program is designed to average sequential acquisitions and can be run via an input variable from a LabVIEW interface specifying the number of averages and an output variable array for the averaged signal. The quad core Xeon processor and high-throughput PCIe interface to the card allow for continuous real time averaging. For each fixed value of the delay time T between the excitation pulses that is set by a LabVIEW interface, this C++ program is called to acquire and average repetitions ranging in number from 1 to 1 million. A similarly averaged background is obtained by turning off the first excitation pulse. The averaged output files from the C++ program are saved to disk by LabVIEW. A Mathematica program reads all the averaged files within that output folder and populates arrays for the excitation and background pulses, respectively. To generate the echo intensity, the Mathematica program subtracts the background from the signal trace, then squares and integrates over a ~ 50 -ns window centered on the echo signal. Under optimal operating conditions, a decay of the echo signal is recorded by varying the pulse separation T in randomized increments of 1 ns over 300 discrete values, and acquiring 50 000 repetitions for each of these points. The decay time constant is obtained on the basis of an exponential fit to the echo signal. For such a 300-point data set, each signal and background trace is acquired in 50 ms, and the pulse generator delays are configured via a GPIB interface in 60 ms between each acquisition. This results in an acquisition time of 220 ms per data point, and a total time of 66 s for the entire data set.

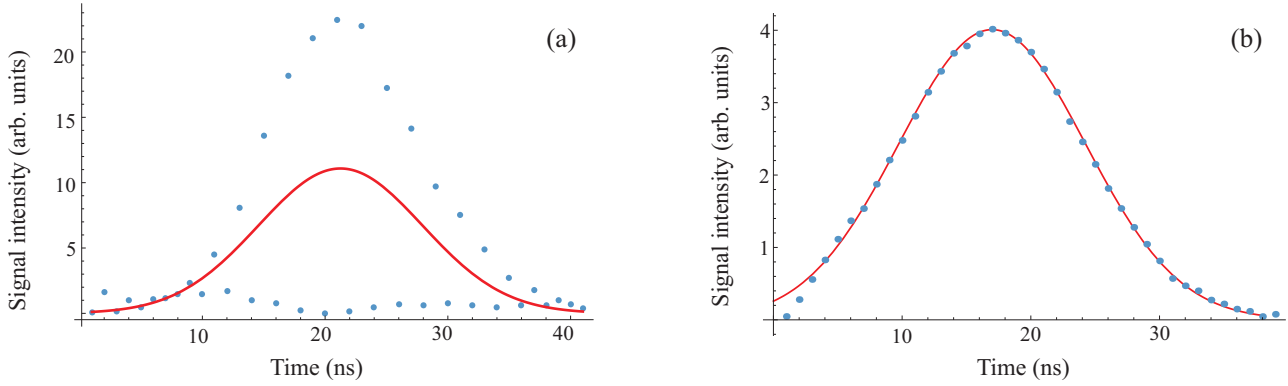


FIG. 3. Digitized trace of the squared echo signal obtained with heterodyne detection (a) and echo envelope obtained with PMT detection (b). The Gaussian fit in part (a) gives a $1/e^2$ width of (26.6 ± 1.4) ns and the fit in part (b) gives a $1/e^2$ width of (28.4 ± 0.1) ns. Although the signal widths in parts (a) and (b) are similar, the two traces were recorded with different excitation pulse widths, and cannot be directly compared.

IV. RESULTS AND DISCUSSION

Figure 3 shows the digitized trace of the squared echo signal recorded with heterodyne detection in part (a), and the echo envelope obtained with PMT detection in part (b). Here, both traces, which have dimensions of intensity, have been recorded using a data card with a sampling time of 1 ns. Since the heterodyne signal consists of a 250-MHz beat note and the squared signal has a 500-MHz frequency, the frequency components of the modulated echo pulse are within a few tens of MHz from the Nyquist frequency of 500 MHz. Therefore, the sampled data and the integrated area under the echo envelope are represented accurately. Since the integrated area under the echo envelope is proportional to the radiated energy, this quantity is determined by fitting a Gaussian to the data and finding the area under the Gaussian within a specified integration window. The lifetime is obtained by plotting the area as a function of $2T$. The duration of the echo signal in Fig. 3 represents the inverse of the fraction of the Doppler-broadened profile excited by the pulse bandwidth as described in Sec. II. We find that the $1/e^2$ fit values of 26.6 and 28.4 ns obtained from Figs. 3(a) and 3(b), respectively, are generally consistent with the width of the signal predicted by the square

of Eq. (3). However, the heterodyne and PMT traces cannot be directly compared, since they result from different excitation pulse widths. Figure 3(b) also shows a slight asymmetry, an effect that arises because the PMT cannot be completely shielded from the excitation pulses due to the rise time of the gate AOM.

Figure 4(a) shows the echo decay on a log scale with a linear fit. This data set, which consists of 300 points each averaged 50 000 times, was obtained with heterodyne detection on a time scale of ~ 1 min. As a check, the same data were also fit to an exponential decay on a linear scale. It was verified that both fits, extending over ~ 4 lifetimes, give consistent values for τ_1 within error bars. The measurement precision of 0.3% is adequate for obtaining accuracies comparable to the measurements in Table I. For these conditions, the peak value of the echo signal corresponds to a power of $80 \mu\text{W}$, based on the calibration of the heterodyne detector. The normalized residuals in Fig. 4(b), determined by $(\text{data} - \text{fit})/\text{fit}$, indicate that the signal-to-noise ratio is ~ 5 , even for the last data point ($T \sim 90$ ns). In comparison, we find that the signal-to-noise ratio of exponential decays recorded with the PMT is ~ 5 times smaller due to the lower dynamic range compared

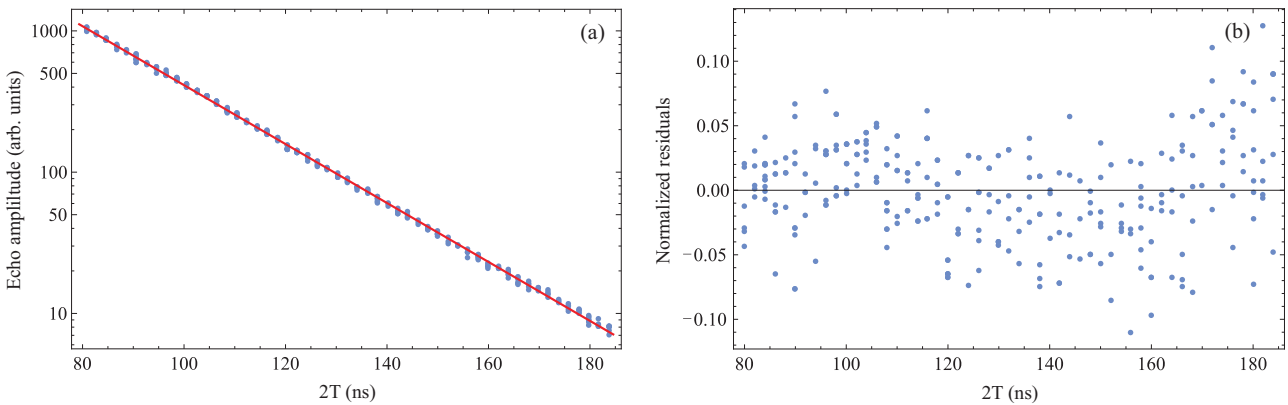


FIG. 4. (a) Decay of the echo signal recorded with heterodyne detection displayed on a log scale. Here, the lifetime inferred from the slope of the linear fit on the basis of Eq. (5) in Sec. II is $\tau_1 = (26.11 \pm 0.08)$ ns, and the intercept is (1076 ± 1) arb. units. (b) Corresponding normalized residuals of part (a).

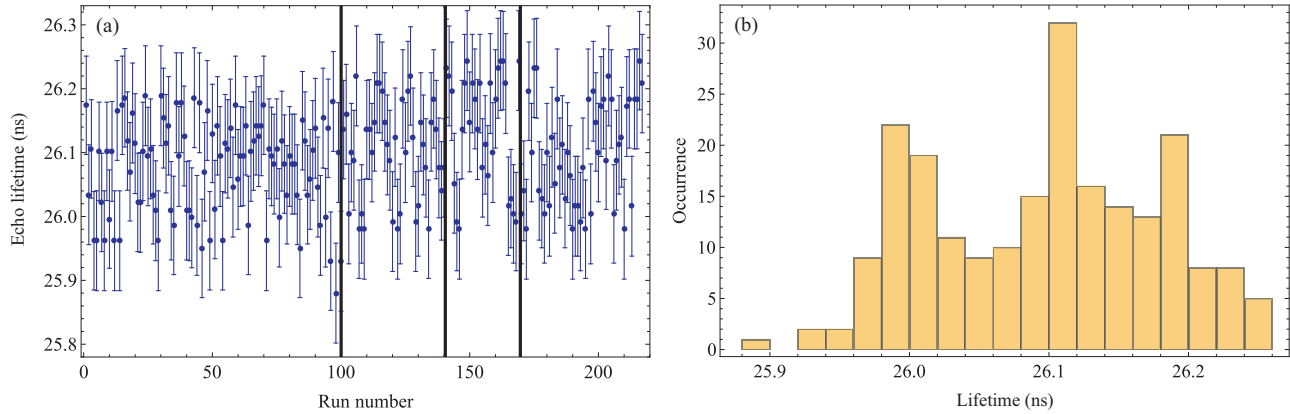


FIG. 5. (a) Sequence of 217 lifetime measurements recorded in 4 h, with τ_1 inferred from exponential fits. The vertical lines indicate the demarcation between four data runs in which data points were taken in an uninterrupted sequence. The typical size of the fit error bars is 0.3%. (b) A histogram of the data presented in part (a). The standard deviation of 0.35% is comparable to the fit error.

to the heterodyne measurement. Other complicating factors associated with PMT detection include worse background subtraction compared to the heterodyne technique—an effect that arises because the PMT’s response is affected by the preceding excitation pulses. As a result, we rely only on the heterodyne technique for the rest of the measurements discussed in this paper. We also note that the excitation scheme that we have used can result in quantum beats between the coherences associated with the Rb excited states. The slowest possible beat note based on hyperfine splittings is 63 MHz, corresponding to a period of 16 ns. However, we have not detected any evidence for such beat notes in the echo envelope or the echo decay.

Figure 5(a) shows a sequence of 217 lifetime measurements recorded over the course of several weeks over four runs using the same data acquisition protocol as in Fig. 4. Each point corresponds to an exponential decay recorded in 66 s, resulting in a total acquisition time of 4 h. These data sets were selected because any deviations from exponential behavior due to sinusoidal variations (discussed later) were smaller than a preset range. Additionally, these measurements were carried out in a “double-blind” manner, in which the value of the lifetime was not only hidden, but also multiplied by a scale factor that was revealed after the data was processed. Figure 5(b) shows a histogram of the measurements from part (a) based on the parameters of the exponential fits. The mean value of these measurements is 26.09 ns, and the standard deviation of 0.09 ns corresponds to a statistical uncertainty of 0.3%. We note that the error bars of the exponential fits in Fig. 5(a) are comparable to this value.

We obtain a rigorous estimate of the uncertainty by computing the variances of the four individual runs in Fig. 5(a). For each run, the statistical uncertainty is determined by calculating the ADEV, fitting to a $\tau^{-1/2}$ power law, and taking its extrapolated value at the last data point on the ADEV curve, as discussed further in the context of Fig. 6. The average values of the four runs shown in Fig. 5(a) and their corresponding statistical uncertainties based on the extrapolated fit values are (26.08 ± 0.01) ns, (26.101 ± 0.008) ns, (26.14 ± 0.01) ns, and (26.10 ± 0.03) ns, respectively, which result in an overall average of $\tau = 26.11$ ns. We calculate the standard variance

of the four runs to be 0.0005 ns². The average of the statistical variances of the four runs is 0.0003 ns². We then obtain a standard deviation of 0.03 ns from the square root of the total variance, which represents the statistical error in the measurement. The final result of $\tau_1 = (26.11 \pm 0.03)$ ns (statistical precision of 0.11%) is the best estimate of the lifetime value of our results, which omits the effects of technical limitations. Furthermore, our estimate of the statistical uncertainty is more conservative than the value given by the standard deviation of the mean of the 217 data points. We also find that none of the experimental parameters that could affect the signal—such as number density, pulse areas, magnetic fields, and polarization—produce changes in the lifetime values that are larger than this best estimate.

Figure 6 shows the ADEV of the longest uninterrupted data run (the first 100 points) included in Fig. 5(a). A $\tau^{-1/2}$ power-law fit to these data results in an extrapolated value of 3.4×10^{-4} at 3300 s. This value represents the best statistical uncertainty that can be achieved by the current configuration of the experiment, namely 0.03%. This analysis suggests that

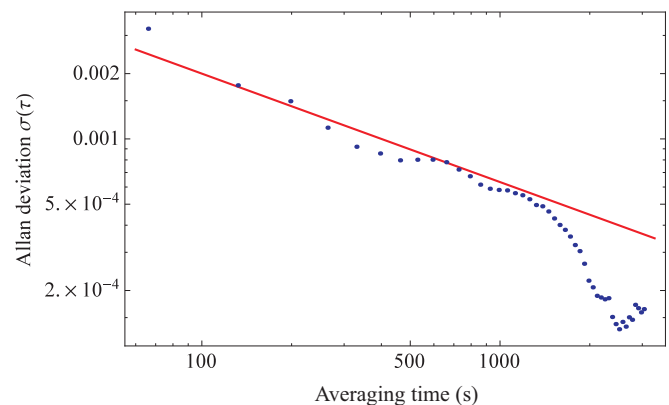


FIG. 6. ADEV of the longest data run of 100 points from the data set in Fig. 5. A $\tau^{-1/2}$ power-law fit is shown for reference. The extrapolated value based on this fit is 3.4×10^{-4} at 3300 s. The vertical axis represents the fractional stability based on the measured lifetime value.

the technical limitations need to be decreased by a factor of ~ 4 to reduce the statistical precision below that of the best lifetime measurement (0.007%) [4]. This shows the viability of the photon echo technique for obtaining the best lifetime measurement if the technical limitations that produce long-term measurement instabilities can be understood and addressed.

The estimated collisional rate of 10 s^{-1} in the vapor cell shows that the dominant systematic effect that can be anticipated is transit time broadening. We use the measured transit time broadening parameter of $4.1 \mu\text{s}/\text{mm}$ for ground-state coherences in a similar vapor cell experiment [32] to estimate the corrected value of the lifetime τ_{corr} . This broadening parameter is consistent with the model used in Refs. [27,33,34]. The transit time τ_{transit} for the average beam diameter used in this work is estimated to be $5.1 \mu\text{s} \pm 10\%$. Following Ref. [34] in the limit that $T \ll \tau_{\text{transit}}$, we obtain $1/\tau_1 = 1/\tau_{\text{corr}} + T/\tau_{\text{transit}}^2$. For an average value of $2T = 130 \text{ ns}$, we obtain $\tau_{\text{corr}} = (26.11 \pm 0.03) \text{ ns}$, which represents a negligible transit-time correction. This value for the $5P_{3/2}$ lifetime agrees to better than 1σ with Ref. [5], as indicated in Table I, but it disagrees with the values reported in Refs. [6,8]. Furthermore, all these measurements agree with the best theoretical calculations for this Rb transition [3], and disagree with previously determined theoretical values [1,2]. A more rigorous estimate of the transit time correction can be obtained by measuring the lifetime over a range of beam diameters.

Another factor that can potentially influence the lifetime measurement is laser phase noise, which produces a decoherence on a time scale τ_{phase} , so that $1/\tau_1 = 1/\tau_{\text{corr}} + T/\tau_{\text{transit}}^2 + 1/\tau_{\text{phase}}$. Although the short-term linewidth of seed lasers used in our work is $\sim 200 \text{ kHz}$ on a time scale of 50 ms (coherence time of $5 \mu\text{s}$), it is dominated by “white” current frequency noise [35], suggesting that contributions of intrinsic Gaussian phase noise occur on time scales longer than $5 \mu\text{s}$. However, the phase-noise contribution can only be estimated on the basis of a direct measurement.

V. ANALYSIS OF TECHNICAL LIMITATIONS

We now explain the technical limitations that preclude studies of systematic effects. Figure 7 shows an example of a single data run of 100 consecutive lifetime measurements with no change in experimental conditions. In this data set, the lifetime values show larger changes than indicated by the size of the error bars, showing that some instability was present. We investigated a number of possible causes for this effect. First, it was suspected that the effect was caused by decoherence due to background light. To verify this, we operated the downstream AOM in the Bragg regime so that the divergence angle of the focused laser beam was smaller than the diffraction angle, thereby reducing the amount of background light passing through the vapor cell. Under these conditions, the $1/e^2$ full width of the excitation pulses was 20 ns . However, this change in alignment did not reduce the lifetime measurement instabilities. We also measured the background light in both configurations of the downstream AOM over several hours and determined that the maximum power level due to background light was $5 \mu\text{W}$. Since these

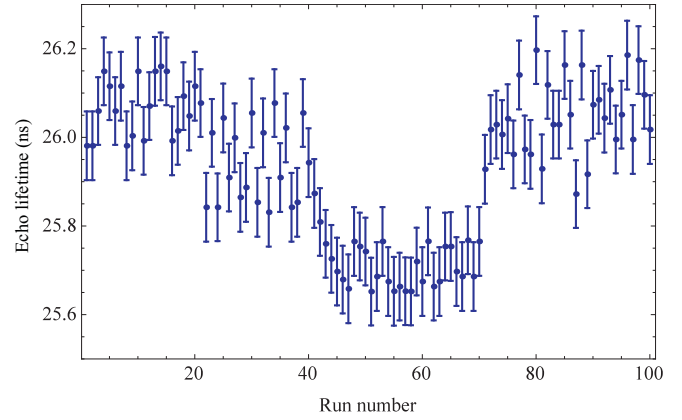


FIG. 7. Data set showing 100 sequential measurements of the lifetime that exhibits an instability of $\sim 0.5 \text{ ns}$. This data set was obtained on a time scale of $\sim 2 \text{ h}$.

photons are associated with the LO, which is 250 MHz upshifted with respect to the excitation beam, we also varied the lock points of the ECDL across the Doppler profile. However, using different lock points did not change the $5\text{-}\mu\text{W}$ background level. The largest excitation probability due to the background photons over the duration of the experiment was $\sim 1.2 \times 10^{-5}$, suggesting that the lifetime variations were not caused by background light related to changes in alignment or changes in detuning. Studies with a Fabry-Perot cavity with a resolution of 50 MHz ruled out any multimode behavior of the laser. Any dependence on the heterodyne detection scheme—such as the effects of mirror vibrations—was ruled out by the observation of similar lifetime variations using a PMT to measure the echo intensity. Although estimates of the changes in the index of refraction of the AOM crystal due to thermal effects were negligible, we also carried out measurements with a thermally stabilized AOM, and found that the lifetime variations persisted.

Since our experimental investigations showed that the measurement instabilities were not related to decoherence, we focused on the effect of imperfect background subtraction of the excitation pulse tails and their interference with the atomic response. This background is dependent on the value of the pulse separation T , as well as slowly varying optical phase due to beam pointing—an effect that is associated with the AOM cavity. Additionally, an interference effect is produced by the slow phase variation associated with the residual rf pulse and the ring-down of the AOM cavity following the application of short pulses, which results in a modulated optical background. We now present a simple model of this effect, which is highly relevant to short-pulse, time-domain spectroscopy using optical switches such as AOMs.

For the heterodyne configuration, we model the total electric field at time t as a superposition of the electric fields of the two excitation pulses and the electric field of the echo pulse, given by

$$E_{\text{tot}}(t) = E_1(t) + E_2(t) + E_e(t). \quad (6)$$

Each pulse is defined by

$$E_i(t) = A_i(t) \cos[\omega t + \phi_i(t)], \quad (7)$$

where the $E_i(t)$ are the electric fields of the first excitation pulse, the second excitation pulse, and the echo, with $i = 1$, $i = 2$, and $i = e$, respectively. Each pulse is described by its amplitude $A_i(t)$ which reaches a maximum at $A_1(0)$, $A_2(T)$, and $A_e(2T)$. The phase $\phi_i(t)$ represents all contributions due to mirror vibrations, laser phase noise, and AOM phase drifts that might occur during the data acquisition time. Both $A_i(t)$ and $\phi_i(t)$ are assumed to be slowly varying functions over the time scale of the period of one rf cycle (4 ns).

At the time of the echo $t = 2T$, the total electric field is therefore

$$E_{\text{tot}}(2T) = E_1(2T) + E_2(2T) + E_e(2T). \quad (8)$$

Since the background signal is obtained by turning off the first excitation pulse, it is described by the electric field of the second excitation pulse $E_2(2T)$. As a result of the background-subtraction procedure, the electric field is given by

$$\begin{aligned} E_{\text{bkg-sub}}(2T) &= E_1(2T) + E_e(2T) \\ &= A_1(2T) \cos[\omega t + \phi_1(2T)] \\ &\quad + A_e(2T) \cos[\omega t + \phi_e(2T)] e^{-T/\tau_1}, \end{aligned} \quad (9)$$

where the phenomenological decay rate $1/\tau_1$ is written explicitly as the decay of the amplitude following e^{-T/τ_1} . Because the data are processed by squaring the signal, the corresponding background-subtracted intensity is

$$\begin{aligned} I(2T) &= A_1^2(2T) \cos^2[\omega t + \phi_1(2T)] \\ &\quad + A_e^2(2T) \cos^2[\omega t + \phi_e(2T)] e^{-2T/\tau_1} \\ &\quad + 2A_1(2T)A_e(2T) e^{-T/\tau_1} \cos[\omega t + \phi_1(2T)] \\ &\quad \times \cos[\omega t + \phi_e(2T)]. \end{aligned} \quad (10)$$

The heterodyne signal is obtained from the time average of Eq. (10) over the period of one rf cycle. The time average of the first two terms in Eq. (10) gives $\frac{1}{2}A_1^2(2T)$ and $\frac{1}{2}A_e^2(2T)e^{-2T/\tau_1}$, respectively. Using the trigonometric identity $2 \cos A \cos B = \cos(A + B) + \cos(A - B)$, the time average of the last term in Eq. (10) becomes

$$\begin{aligned} A_1(2T)A_e(2T) e^{-T/\tau_1} \int_{0 \text{ ns}}^{4 \text{ ns}} \{ \cos[2\omega t + \phi_1(2T) + \phi_e(2T)] \\ + \cos[\phi(2T)] \} dt, \end{aligned} \quad (11)$$

where $\phi(2T) = \phi_1(2T) - \phi_e(2T)$. The integral of the first term, which is modulated at twice the optical frequency, gives zero; the second term, which is constant over the 4-ns period, only varies on longer time scales. Equation (11) then becomes

$$A_1(2T)A_e(2T) e^{-T/\tau_1} \cos[\phi(2T)]. \quad (12)$$

As a result, the intensity of the background-subtracted signal given in Eq. (10) becomes

$$\begin{aligned} I(2T) &= \frac{1}{2}A_1^2(2T) + \frac{1}{2}A_e^2(2T) e^{-2T/\tau_1} \\ &\quad + A_1(2T)A_e(2T) e^{-T/\tau_1} \cos[\phi(2T)]. \end{aligned} \quad (13)$$

The result of Eq. (13) shows that the decay intensity of the echo signal as a function of time is modulated by a slowly varying background $\cos[\phi(2T)]$ which decays as e^{-T/τ_1} , does

not subtract out, and is the likely cause for the lifetime deviations.

To further explore the predictions of the model, we have simulated the exponential decay based on Eq. (13) using data from a measured pulse of amplitude $A_2(t)$. Figure 8(a) shows a typical optical pulse generated by the AOM and measured with heterodyne detection. Ring-down effects after the pulse generate a slowly decaying tail at the natural resonance frequency of the AOM (~ 227 MHz). The beat note between the tail and the 250-MHz heterodyne signal produces a modulation which is not removed by the background-subtraction procedure. Therefore, the modulation can appear on the exponential decay as an added oscillation at the beat frequency, as shown in Fig. 8(b).

For the simulation, we use $A_1(t) = c_1 A_2(t + T)$ and $A_e(t) = c_2 e^{-i\phi} A_2(t - T)$, where c_1 , c_2 , and ϕ are constants derived from experimental conditions. Depending on the relative phase between the rf, acoustic, and optical signals, the deviation from an exponential fit will have an amplitude which is sensitive to alignment, and produce lifetime measurement instabilities on long time scales. The simulated data in Fig. 8(b) shows an example where the deviation from an exponential decay is significant. This effect is once again emphasized in Fig. 8(c), which shows the normalized fit residuals, namely (data - fit)/fit, so that the deviations from an exponential decay are readily apparent. These deviations arise from the last term of Eq. (13) with a phase $\phi = -0.875$ between the pulse amplitudes A_e and A_2 . For this particular data set, the measured lifetime is 25.7 ns, but phase instabilities as small as $\Delta\phi \sim 0.05$ result in varying values, in agreement with Fig. 7.

The theoretical model and the simulations are corroborated by the experimental data in Fig. 9(a), which shows an example of a decay measured with heterodyne detection, where a deviation from an exponential is clearly apparent. This data set is also an example that did not meet the selection criteria for the 217 data sets in Fig. 5, due to the size of the oscillating ripples. Figure 9(b) shows the relative residuals. Here, the model predicts that such a large oscillating background can significantly modify the exponential fit, and thus the measurement must be rejected. Conversely, when deviations from an exponential are smaller than the level of noise, the last term of Eq. (13) is small and the lifetime value is not affected. This is the criterion that was used to choose the data sets of Fig. 5. However, this method has its limitations, as even a small deviation from an exponential decay can affect the measured lifetime. This is seen to cause variations of the lifetime by as much as ± 0.1 ns in the data set of Fig. 5 (for example data points between run numbers 30 to 50). The criterion therefore selects data that can have a systematic error as large as ~ 0.1 ns.

A similar model for Eq. (8) for PMT detection is given by Eq. (14) [36]:

$$\begin{aligned} I(2T) &= \frac{1}{2}A_2^2(2T) + \frac{1}{2}A_e^2(2T) e^{-2T/\tau_1} \\ &\quad + A_1(2T)A_2(2T) \cos[\phi'(2T)] \\ &\quad + A_1(2T)A_e(2T) e^{-T/\tau_1} \cos[\phi(2T)] \\ &\quad + A_2(2T)A_e(2T) e^{-T/\tau_1} \cos[\phi''(2T)], \end{aligned} \quad (14)$$

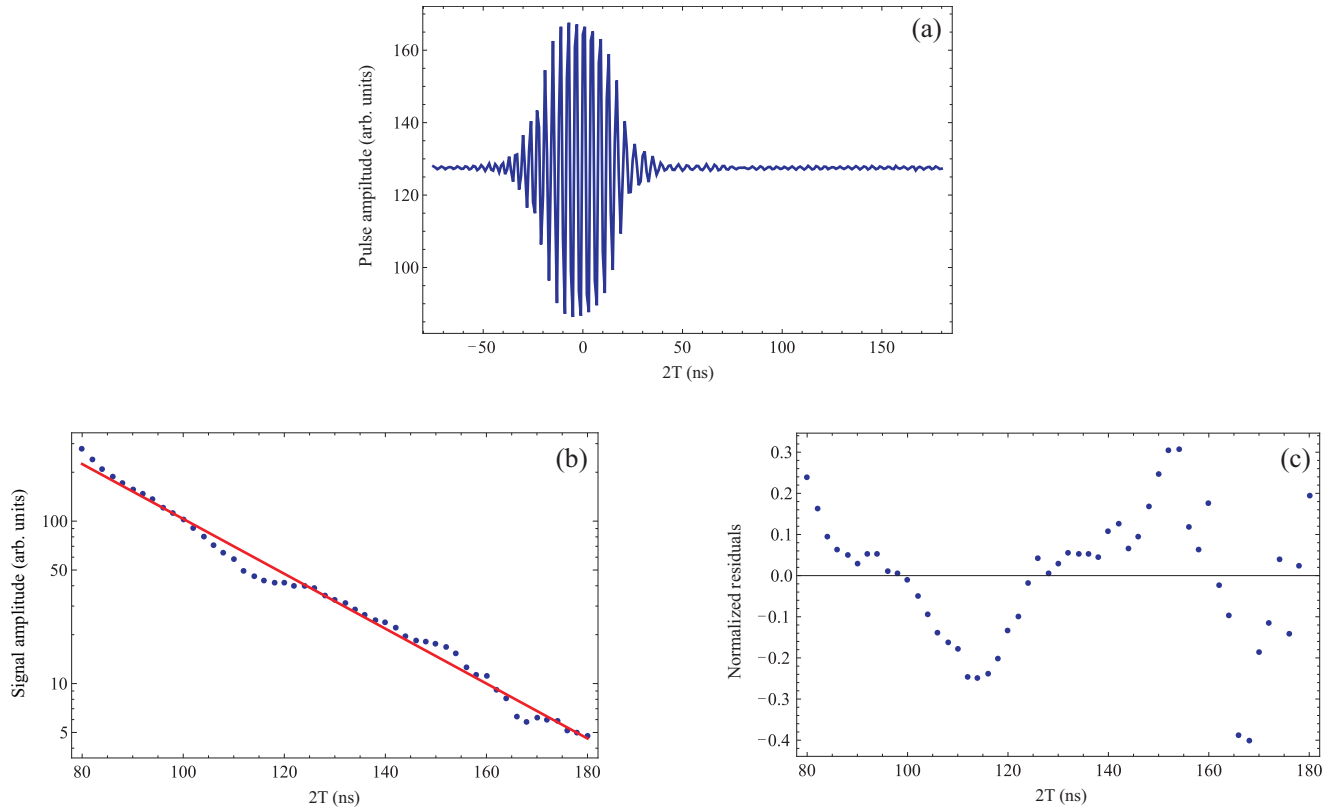


FIG. 8. (a) Typical optical pulse generated by the AOM and measured with the heterodyne detection setup. This pulse represents the amplitude term $A_2(t)$ in Eq. (7) and is used to simulate the effects of AOM pulse tails on the lifetime measurements. (b) Simulation of an exponential decay measurement of the echo signal based on Eq. (13). The pulse amplitudes $A_1(t)$ and $A_e(t)$ are derived from the measured pulse $A_2(t)$ shown in part (a). By adjusting the amplitude and phase of $A_e(t)$, different values for the measured lifetime are obtained. For this particular example, $\tau_1 = 26.1$ ns, $A_e(t) = -0.67e^{-0.875t}A_2(t - T)$, and the fitted lifetime value is 25.7 ns. (c) Normalized residuals—obtained by subtracting the fit from the data and dividing by the fit—show a clear deviation from the exponential decay.

where $\phi'(2T) = \phi_1(2T) - \phi_2(2T)$, $\phi(2T) = \phi_1(2T) - \phi_e(2T)$ (as defined previously in the heterodyne treatment), and $\phi''(2T) = \phi_2(2T) - \phi_e(2T)$. The result of Eq. (14) shows that the background-subtracted signal in PMT detection is even more complicated. This is because intensity detection requires the squaring of the electric fields before background subtraction. The results of this model are well supported by the experiment, since we consistently find that background

subtraction works better for heterodyne detection. This aspect of the detection was further emphasized by studies of the background subtraction carried out without the presence of the Rb cell. Other indirect evidence that supports this model is the behavior of the background offset parameter of the exponential fits, which represents an average variation in the background over the entire exponential decay. This fit parameter is strongly correlated with the lifetime

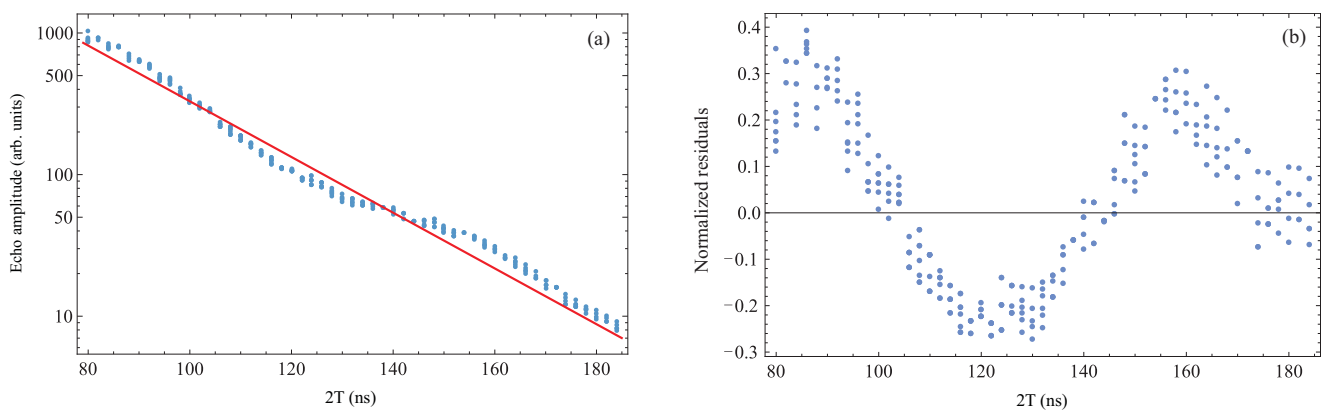


FIG. 9. (a) An example of the exponential decay of the echo signal plotted on a log scale. The exponential fit gives $\tau_1 = (26.1 \pm 0.2)$ ns. (b) Normalized fit residuals of the data in part (a).

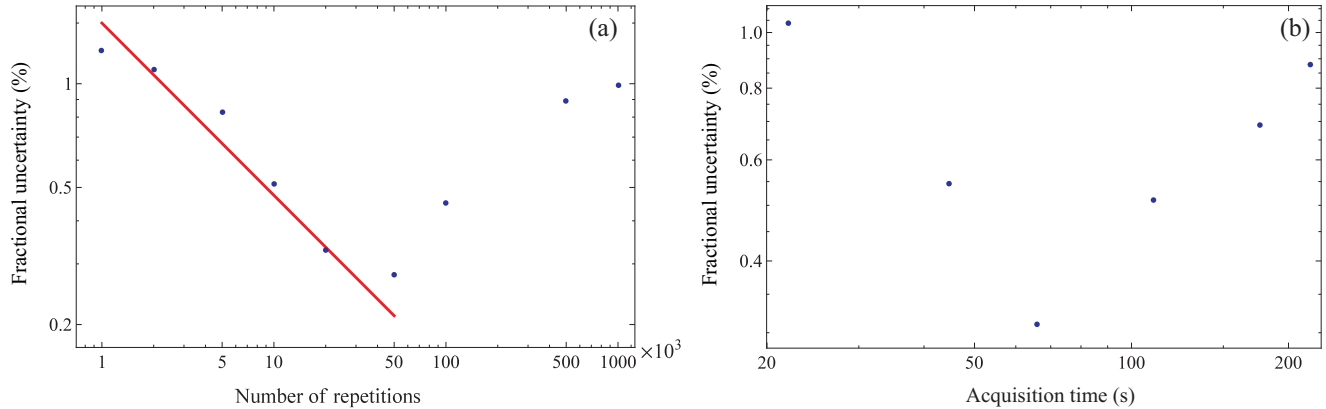


FIG. 10. (a) Fractional uncertainty in the lifetime values from single exponential fits recorded with heterodyne detection as a function of the number of repetitions (averaging time) for each point on the exponential decay. The averaging time varied from 1 ms for 1000 repetitions to 1000 ms for 1 000 000 repetitions. The fit line represents an inverse square-root dependence. (b) Fractional uncertainty in the lifetime values from single exponential fits recorded with heterodyne detection as a function of the number of points on each exponential decay. For all data points on this plot, the number of repetitions was fixed at 50 000. The acquisition time varied from 22 s for 100 points to 220 s for 1000 points. Both data sets exhibit minima corresponding to the optimal operating conditions for the experiment, namely 50 000 acquisitions with 300 points on the exponential decay.

measurement variations for PMT detection, and weakly correlated for heterodyne detection.

The effects described by the model are further emphasized by a plot of the fractional uncertainty of the lifetime recorded by varying the number of repetitions for each point on the exponential decay, and the number of points on the decay curve, as shown in Figs. 10(a) and 10(b), respectively. In both these figures, the fractional uncertainty with respect to the lifetime value is determined from the fit error of a single exponential decay. In Fig. 10(a), the number of points on the exponential decay was fixed at 300, and the averaging time varied from 1 ms for 1000 repetitions to 1000 ms for 1 000 000 repetitions. The reduction in the fractional uncertainty exhibits an inverse square-root dependence (fit line) until the optimum number of repetitions (50 000) is reached. The turning point at 50 000 repetitions indicates the contributions of long-term effects due to optical and rf phase variations. The increase in the fractional uncertainty is dominated by the long time scale noise (up to 1 s) represented by the modulated phase term in Eq. (13). The fractional uncertainty in Fig. 10(b), which was recorded by incrementing the number of points on the decay curve from 100 to 1000, shows that the optimum number of points corresponds to 300. Here, the number of repetitions for each point on the exponential decay was fixed at 50 000 so that the acquisition time varied from 22 to 220 s. It is evident that the long-term instabilities continue to dominate on time scales extending to several minutes. The results from Fig. 10 for the best fractional uncertainty in the lifetime values from exponential fits (0.28%) are consistent with our best estimate for the statistical error of a single exponential fit (0.3%).

Our studies show that if the long-term phase variations are addressed, the inverse square-root dependence in Fig. 10(a) will result in a statistical precision of 0.03% for a single exponential decay with 1 million repetitions (corresponding to a total acquisition time of 636 s for 300 points on the exponential curve). Such conditions would allow rigorous investigations of possible systematic effects due to excita-

tion pulse parameters, polarization, magnetic fields, and cell density.

Although the model we have presented is simple, it provides insight into how the measurement instabilities can be reduced in a future experiment, as outlined in Fig. 11. Here, we envision a heterodyne beat note that can be generated in real time in a separate reference interferometer without the presence of a Rb cell. For each value of T , the time-averaged beat note in the reference interferometer can be subtracted from the time-averaged echo signal. The subtraction of these two signals would eliminate the first two terms in Eq. (6), so that only the echo term survives. To ensure that the subtraction works well for all T values and on long time scales, both interferometers must have the same relative phase. To achieve this outcome, we propose controlling the optical phase in the reference interferometer with a piezo-mounted mirror with a response time of ~ 50 ms so that it is faster than the time scale of any anticipated phase variations. A correction signal obtained by mixing the two heterodyne beat notes and integrating the resulting DC signal can be fed back to the piezo to ensure the necessary long-term stability.

VI. CONCLUSIONS

This work explores the advantages of the photon echo technique for achieving accurate measurements of atomic lifetimes. We have obtained a transit-time corrected value of 26.11 ns with a statistical uncertainty of 0.03 ns (0.11%) in 4 h of data acquisition over several weeks for the ^{85}Rb $5P_{3/2}$ lifetime. This determination is consistent with the value reported in Ref. [5], but it disagrees with the results of Refs. [6,8]. Furthermore, our best estimate of the statistical uncertainty of 0.03% from the extrapolated ADEV value is approximately a factor of 4 larger than the statistical uncertainty of the best lifetime measurement [4], which is indicative of the potential of the data acquisition with a large repetition rate available with the photon echo technique. Our studies of the technical

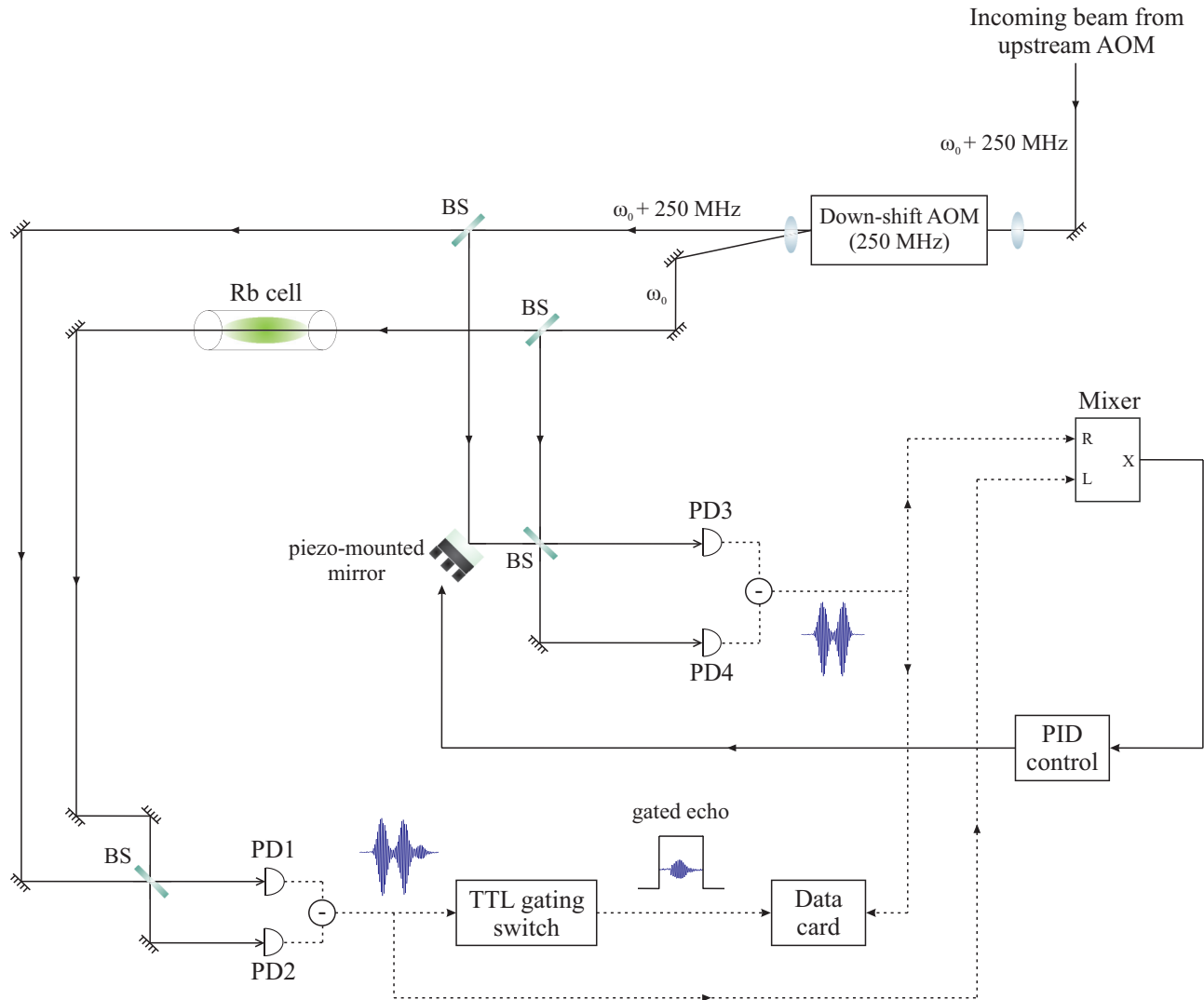


FIG. 11. Proposed experimental setup for mitigating long-term measurement instabilities. The signal from a separate heterodyne alignment without the presence of a Rb cell would be mixed with the signal containing the echo and fed back to a piezo-mounted mirror to correct for mirror vibrations and long-term phase variations.

limitations supported by a simple model suggest that the long-term stability is related to eliminating the tails of optical excitation pulses. The use of higher-frequency AOMs with suitable impedance-matched resonant cavities and rf switches with faster settling times can realistically reduce the excitation pulse widths by approximately a factor of 2. However, such improvements do not sufficiently eliminate the pulse tails, suggesting that the feedback loop we have outlined based on our model offers a more effective solution for reducing the observed measurement instabilities. Studies of the fractional uncertainty in the lifetime value show that the advantages of the high repetition rate can be fully exploited to achieve a statistical precision of 0.03% for a single exponential decay recorded over ~ 10 min if the long-term stability is improved. Exploration of systematic effects at such a level would open the possibility for comparative measurements of the $5P_{3/2}$ and $5P_{1/2}$ level for even more precise comparisons with theory that can serve as tests of the standard model. Since the echo technique is generally applicable to low-lying, closed transitions in atomic systems with large oscillator strengths,

it could open the door for a new round of such lifetime measurements. Although the echo technique can achieve even lower fractional uncertainties for longer-lived lifetimes, its applicability to upper-level transitions is possibly limited due to competing coherent optical effects such as superradiance and superfluorescence [37] that also lead to rapid relaxation. However, for specific level schemes, multistep incoherent excitation can at least limit the evolution of super-radiant processes and create conditions for utilizing the echo technique.

ACKNOWLEDGMENTS

This work was supported by Canada Foundation for Innovation, Ontario Innovation Trust, Ontario Centers of Excellence, Natural Sciences and Engineering Research Council of Canada, and York University. We acknowledge helpful discussions with E. Rotberg and B. Barrett. We also thank an anonymous referee whose comments and suggestions helped improve and clarify this manuscript.

- [1] M. S. Safronova, W. R. Johnson, and A. Derevianko, *Phys. Rev. A* **60**, 4476 (1999).
- [2] M. S. Safronova, C. J. Williams, and C. W. Clark, *Phys. Rev. A* **69**, 022509 (2004).
- [3] M. S. Safronova and U. I. Safronova, *Phys. Rev. A* **83**, 052508 (2011).
- [4] W. I. McAlexander, E. R. I. Abraham, and R. G. Hulet, *Phys. Rev. A* **54**, R5 (1996).
- [5] J. E. Simsarian, L. A. Orozco, G. D. Sprouse, and W. Z. Zhao, *Phys. Rev. A* **57**, 2448 (1998).
- [6] U. Volz and H. Schmoranzner, *Phys. Scr.* **T65**, 48 (1996).
- [7] C. W. Oates, K. R. Vogel, and J. L. Hall, *Phys. Rev. Lett.* **76**, 2866 (1996).
- [8] R. F. Gutterres, C. Amiot, A. Fioretti, C. Gabbanini, M. Mazzoni, and O. Dulieu, *Phys. Rev. A* **66**, 024502 (2002).
- [9] C. E. Tanner, A. E. Livingston, R. J. Rafac, F. G. Serpa, K. W. Kukla, H. G. Berry, L. Young, and C. A. Kurtz, *Phys. Rev. Lett.* **69**, 2765 (1992).
- [10] L. Young, W. T. Hill, III, S. J. Sibener, S. D. Price, C. E. Tanner, C. E. Wieman, and S. R. Leone, *Phys. Rev. A* **50**, 2174 (1994).
- [11] S. A. Blundell, W. R. Johnson, and J. Sapirstein, *Phys. Rev. A* **43**, 3407 (1991).
- [12] V. A. Dzuba, V. V. Flambaum, A. Y. Krafmakher, and O. P. Sushkov, *Phys. Lett. A* **142**, 373 (1989).
- [13] S. Svanberg and S. Rydberg, *Z. Phys.* **227**, 216 (1969).
- [14] S. Rydberg and S. Svanberg, *Phys. Scr.* **5**, 209 (1972).
- [15] J. Marek and P. Munster, *J. Phys. B: At. Mol. Phys.* **13**, 1731 (1980).
- [16] N. Bendali, H. T. Duong, and J. L. Vialle, *J. Phys. B: At. Mol. Phys.* **14**, 4231 (1981).
- [17] Y. C. Chen, K. Chiang, and S. R. Hartmann, *Phys. Rev. B* **21**, 40 (1980).
- [18] R. Macfarlane and R. Shelby, *Opt. Commun.* **39**, 169 (1981).
- [19] P. C. Becker, H. L. Fragnito, C. H. Brito Cruz, R. L. Fork, J. E. Cunningham, J. E. Henry, and C. V. Shank, *Phys. Rev. Lett.* **61**, 1647 (1988).
- [20] A. Flusber, T. Mossberg, and S. Hartmann, *Opt. Commun.* **24**, 207 (1978).
- [21] C. K. N. Patel and R. E. Slusher, *Phys. Rev. Lett.* **20**, 1087 (1968).
- [22] D. A. Wiersma, *Adv. Chem. Phys.* **47**, 421 (1981).
- [23] I. D. Abella, N. A. Kurnit, and S. R. Hartmann, *Phys. Rev.* **141**, 391 (1966).
- [24] L. Allen and J. H. Eberly, *Optical Resonance and Two-level Atoms* (Wiley, New York, 1975).
- [25] G. W. Biedermann, H. J. McGuinness, A. V. Rakholia, Y.-Y. Jau, D. R. Wheeler, J. D. Sterk, and G. R. Burns, *Phys. Rev. Lett.* **118**, 163601 (2017).
- [26] S. L. McCall and E. L. Hahn, *Phys. Rev.* **183**, 457 (1969).
- [27] E. A. Rotberg, B. Barrett, S. Beattie, S. Chudasama, M. Weel, I. Chan, and A. Kumarakrishnan, *J. Opt. Soc. Am. B* **24**, 671 (2007).
- [28] A. Pouliot, H. C. Beica, A. Carew, A. Vorozcovs, G. Carlse, and A. Kumarakrishnan, *Proc. SPIE* **10514**, 105140S (2018).
- [29] X. H. Qi, L. Yi, Q. L. Ma, D. W. Zhou, X. J. Zhou, and X. Z. Chen, *Appl. Opt.* **48**, 4370 (2009).
- [30] F. C. Cruz, M. C. Stowe, and J. Ye, *Opt. Lett.* **31**, 1337 (2006).
- [31] S. R. Systems, Model PRS10 Rubidium Frequency Standard, 2015, version 1.5.
- [32] A. Kumarakrishnan, U. Shim, S. B. Cahn, and T. Sleator, *Phys. Rev. A* **58**, 3868 (1998).
- [33] J. L. Cohen and P. R. Berman, *Phys. Rev. A* **54**, 5262 (1996).
- [34] J. E. Thomas and R. A. Forber, *Opt. Lett.* **9**, 56 (1984).
- [35] H. C. Beica, A. Pouliot, A. Carew, A. Vorozcovs, N. Afkhami-Jeddi, T. Vacheresse, G. Carlse, P. Dowling, B. Barron, and A. Kumarakrishnan, *Rev. Sci. Instrum.* **90**, 085113 (2019).
- [36] H. C. Beica, Ph.D. thesis, York University, 2019.
- [37] E. Paradis, B. Barrett, A. Kumarakrishnan, R. Zhang, and G. Raithel, *Phys. Rev. A* **77**, 043419 (2008).